

Experimental observation using particle image velocimetry of inertial waves in a rotating fluid

Laura Messio · Cyprien Morize · Marc Rabaud ·
Frédéric Moisy

Received: 11 January 2007 / Revised: 2 October 2007 / Accepted: 2 October 2007 / Published online: 21 October 2007
© Springer-Verlag 2007

Abstract Inertial waves generated by a small oscillating disk in a rotating water filled cylinder are observed by means of a corotating particle image velocimetry system. The wave takes place in a stationary conical wavepacket, whose angle aperture depends on the oscillation frequency. Direct visualisation of the velocity and vorticity fields in a plane normal to the rotation axis are presented. The characteristic wavelength is found to be approximately equal to the disk diameter. The classical dispersion relation for plane waves is verified from the radial location of the wavepacket, and from the ellipticity of the projected velocity diagram.

1 Introduction

A homogeneous fluid rotating at constant angular velocity supports a specific and unusual class of waves which propagate in the interior of the fluid, known as inertial (or gyroscopic) waves (Greenspan 1968; Pedlosky 1987; Cushman-Roisin 1994). These waves are of primary importance in geophysics and astrophysics (oceanic and

atmospheric flows, liquid planet core, rotating stars), in which cases they are often coupled with density stratification effects. Purely inertial waves are also relevant to industrial flows, such as spacecrafts fuel tanks or liquid-filled ballistics. The most striking properties of these waves arise from their anisotropic dispersion, leading to a number of non-intuitive geometrical behaviours, such as an energy propagation normal to the phase velocity and anomalous reflection on solid boundaries (Lighthill 1978; Phillips 1963).

The rationale for these fluid oscillations in the presence of rotation is as follows. In the steady solid-body rotation regime, the radial pressure gradient balances the centrifugal force. This equilibrium is stable: if a fluid particle is displaced outward in the radial direction, its azimuthal velocity in the inertial frame will be lower than the velocity of solid rotation at the new position, because it conserves the angular momentum it had at the original position. The lower centrifugal force at the new position is no longer balanced by the inward pressure gradient, and the fluid particle experiences a restoring force. In the rotating frame, this restoring mechanism is described in terms of the Coriolis force, $\mathbf{F}_c = -2\boldsymbol{\Omega} \times \mathbf{u}$ (per unit mass). In the absence of viscosity, the displaced fluid particle will start to oscillate, describing circles in the sense opposite to that of the background rotation (“anticyclonic” circular translation), with a pulsation 2Ω .

If now a disturbance is forced with a pulsation σ smaller than 2Ω , the fluid particles still describe circles in the rotating frame, but now within oblique planes. The angle θ between the normal to the plane and the rotation axis is such that the in-plane Coriolis force, $2\Omega u \cos\theta$, equals the lower acceleration σu (see Fig. 1a) (Phillips 1963). In addition to the above-mentioned centripetal pressure gradient, a new pressure gradient has to balance the

Electronic supplementary material The online version of this article (doi:10.1007/s00348-007-0410-3) contains supplementary material, which is available to authorized users.

L. Messio · C. Morize · M. Rabaud · F. Moisy
Univ Paris-Sud; Univ Pierre et Marie Curie, CNRS,
Orsay, France

L. Messio · C. Morize · M. Rabaud · F. Moisy (✉)
Fluides, Automatique et Systèmes Thermiques (FAST),
Bâtiment 502, Campus Universitaire, 91405 Orsay, France
e-mail: moisy@fast.u-psud.fr

component of the Coriolis force normal to the plane of motion. Since this plane of motion is a surface of constant phase (i.e. constant velocity and pressure), the pressure gradient results in a colinear phase velocity, so that the fluid motion appears within a transverse circularly polarized travelling wave (Fig. 1b). The anisotropic dispersion of inertial waves follows from this dependence of the wavevector angle upon the pulsation σ .

Depending on whether the characteristic wavelength is large or small compared to the container size, inertial waves may be considered as *global* (or *contained*) or *local* (short wavelength approximation).

The *global* forcing is of primary importance in natural flows in the ocean, atmosphere, or liquid planet cores. In these systems, inertial waves, or more generally inertia-gravity waves, may be forced either by an oscillating homogeneous body force, as for the ocean tides, or from the temporal variation of the background rotation vector, as for the precessing Earth core (Aldridge and Lumb 1987). A number of laboratory experiments of contained inertial waves have been carried out in various geometries of industrial or geophysical relevance, including cylinder (Oser 1958; Fultz 1959; McEwan 1970; Ito et al. 1984; Manasseh 1996; Duguet 2006), cone (Beardsley 1970), spheroids (Malkus 1968), or more complex geometries (Maas 2001; Manders and Maas 2003).

On the other hand, a small oscillating disturbance in an infinite medium provides a *local* excitation of inertial waves. Far from the source, these are essentially plane waves propagating along “rays”, and may display a variety of familiar phenomena of optics, such as reflection, refraction and interference (Lighthill 1978; Phillips 1963).

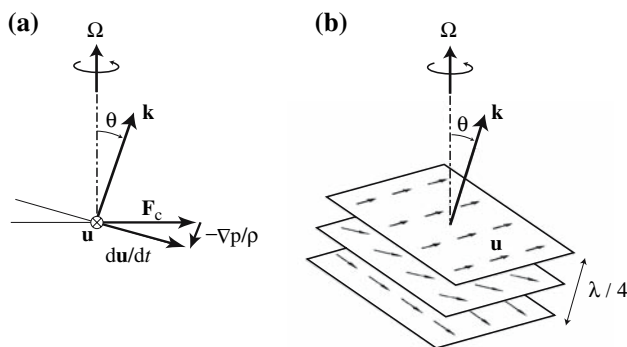


Fig. 1 **a** Coriolis force and pressure gradient experienced by a fluid particle in circular translation with pulsation σ in a frame rotating at angular velocity Ω about the vertical axis. The velocity \mathbf{u} and the acceleration $d\mathbf{u}/dt$ lie in an oblique plane, normal to the wavevector \mathbf{k} making angle $\theta = \cos^{-1}(\sigma/2\Omega)$ to the rotation axis (here \mathbf{u} is chosen normal to Ω). **b** Three planes of constant phase $0, \pi/4, \pi/2$ (corresponding to $1/4$ wavelength), normal to \mathbf{k} , emphasizing the circularly polarized transverse wave and the shearing motion between planes. The phase velocity is along \mathbf{k} , showing that the circular translation is anticyclonic

Visualisations of the flow field emitted from a point source may be found in the numerical study by Godefert and Lollini (1999). Laboratory experiments focusing on such *localized* inertial waves are more sparse than for *global* forcing (Oser 1958). It must be noted, however, that for experiments in a finite container, if the viscous damping is negligible, the observed wave pattern is the result of the interference between multiple reflected waves, so the intended *local* wave may also show *global* properties.

The aim of the present paper is to present simple visualisations of inertial waves forced by a small oscillating disk in a large rotating cylinder, revisiting a classical geometry first investigated by Oser (1958) and Fultz (1959). Although the properties of the inertial waves are already well documented in the literature [see Greenspan (1968) for a review of those early experiments], only qualitative observations of the flow itself, by means of visualisation using dye or anisotropic flakes, have been carried out. In the present paper, particle image velocimetry (PIV) has been used to directly observe the velocity field of the wave produced by a small disturbance. This non intrusive technique has been also used recently by Maas (Maas 2001; Manders and Maas 2003), to investigate the focusing of wave on attractors in closed geometries with sloping boundaries, using a *global* forcing. On the other hand, the small size of the wave source compared to the rotating tank and the significant viscous damping make the present experiment closer to the *local* forcing scheme.

The paper is organized as follows. First the dispersion relation for plane waves and the geometry of the wave-packet are discussed in Sect. 2. The experimental setup and the measurement techniques are described in Sect. 3. In Sect. 4 the velocity fields measured by PIV are described, from which the dispersion relation and the wavelength selection are analyzed. Finally, some concluding remarks are offered in Sect. 5.

2 Theoretical background

2.1 Dispersion relation for plane waves

In this section we briefly derive the dispersion relation for linear plane waves and recall their main properties. We start from the inviscid equation for the vorticity, $\boldsymbol{\omega} = \nabla \times \mathbf{u}$, written in the frame rotating at constant angular velocity Ω ,

$$\frac{\partial \boldsymbol{\omega}}{\partial t} + (\mathbf{u} \cdot \nabla) \boldsymbol{\omega} = [(\boldsymbol{\omega} + 2\Omega) \cdot \nabla] \mathbf{u}, \quad (1)$$

and the continuity equation written for the velocity and the vorticity,

$$\nabla \cdot \mathbf{u} = 0, \quad \nabla \cdot \boldsymbol{\omega} = 0. \tag{2}$$

We consider for convenience $\boldsymbol{\Omega} = \Omega \hat{\mathbf{z}}$ in the z direction. We seek for plane wave solutions for a single Fourier component \mathbf{k} , written in cartesian coordinates,

$$\mathbf{u} = \mathbf{U}_0 e^{i(\mathbf{k} \cdot \mathbf{x} - \sigma t)}, \quad \boldsymbol{\omega} = \mathbf{W}_0 e^{i(\mathbf{k} \cdot \mathbf{x} - \sigma t)}, \tag{3}$$

where \mathbf{U}_0 and $\mathbf{W}_0 = i\mathbf{k} \times \mathbf{U}_0$ are constant complex vectors, both normal to \mathbf{k} due to incompressibility (2), i.e., the wave is transverse. Note here that there is no *rotation* but only *circular translation* of the fluid particles in the plane of motion, so the vorticity here is only associated to the shearing between planes of constant phase (Fig. 1b). For such plane wave, the two nonlinear terms $(\mathbf{u} \cdot \nabla)\boldsymbol{\omega}$ and $(\boldsymbol{\omega} \cdot \nabla)\mathbf{u}$ in Eq. (1) vanish exactly: nonlinear effects may only be expected from a combination of two or more Fourier components.

Inserting Eq. (3) into Eq. (1) gives the relation dispersion for those plane waves,

$$\sigma = 2\Omega \frac{k_z}{k} = 2\Omega \cos \theta \tag{4}$$

where θ is the angle between $\boldsymbol{\Omega}$ and the wave vector \mathbf{k} , yielding the phase velocity,

$$\mathbf{c} = 2\Omega \cos \theta \frac{\mathbf{k}}{k^2}. \tag{5}$$

Inertial waves are therefore dispersive and anisotropic: \mathbf{c} depends both on the magnitude and the angle of the wavevector \mathbf{k} . A remarkable consequence of Eq. (4) is that a given pulsation is not uniquely associated to a wavelength, so that the actual wavelength (or range of wavelengths) of the wave is expected to be selected by an external lengthscale, e.g., the size of a disturbance for a local forcing, or the system size itself for a global forcing.

Equation (5) tells how points of constant phase travel, but does not tell *where* the wave actually takes place, i.e., where the energy of a given disturbance propagates. The velocity of energy propagation is the group velocity which, for plane waves, is given by $\mathbf{c}_g = \nabla_k \sigma$ (Lighthill 1978), where ∇_k is the gradient in wavenumber space, yielding

$$\mathbf{c}_g = \mathbf{k} \times (2\boldsymbol{\Omega} \times \mathbf{k})/k^3, \tag{6}$$

of magnitude $c_g = (2\Omega/k)\sin\theta$. Comparing Eqs. (5) and (6) shows that the phase and group velocities are normal, and satisfy $\mathbf{c} + \mathbf{c}_g = 2\boldsymbol{\Omega}/k$. Physically, this property implies that an instantaneous localized disturbance propagates energy in a wavepacket at velocity \mathbf{c}_g along the direction $\theta_g = \pi/2 - \theta$, and within this wavepacket the phase of the wave travels normal to \mathbf{c}_g . More insight into anisotropic dispersive waves can be found in Lighthill (1978).

2.2 Wavepacket forced by an oscillating source

We now consider the inertial waves emitted from the periodic oscillation of a small source. The details of the flow field in the vicinity of the source may be rather complex, but only the flow far from it is considered here. Plane waves are not exact solutions of the problem, so we restrict here to linear waves of small amplitude, and only a qualitative discussion of the wave pattern is given in the following.

Consider a small source, of characteristic size ℓ , oscillating with pulsation σ and amplitude A (see Fig. 2), initiating a velocity disturbance σA in its vicinity. Since the energy propagates at an angle $\theta_g = \pi/2 - \theta$ from the source, the wave pattern takes place in a wavepacket in the form of a double cone, making an angle θ_g to the rotation

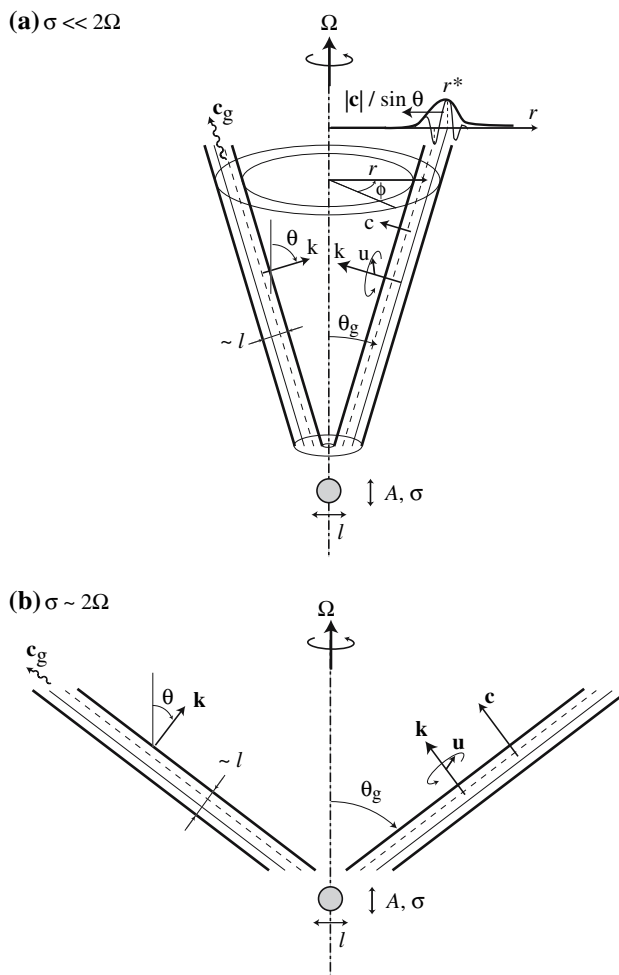


Fig. 2 Sketch of the inertial wave emitted from an oscillating disturbance of size ℓ in an infinite medium. Only the upper half cone is shown. **a** Low pulsation, **b** pulsation comparable to twice the angular velocity 2Ω . The *solid* and *dashed* lines in the conical wavepacket represent two surfaces of constant phase $\alpha = 0$ and $\alpha = \pi$ (a “trough” and a “crest” of a velocity component)

axis (only the upper half cone is shown in Fig. 2). The fluid oscillates inside the thickness of the cone, and is at rest outside. Note that for a finite container the cone axis is parallel but does not necessarily coincide with the rotation axis. For a periodic oscillation, the energy fluxes continuously along this conical wavepacket to infinity, so that the wavepacket is stationary. In the absence of viscosity and for small amplitude A , ℓ is the only lengthscale of the problem, so both the thickness of the cone and the wavelength are expected to be of order of ℓ .

In the far field approximation, where the radius of the cone is much larger than its thickness, the curvature of the cone may be neglected and the above description in terms of plane waves becomes relevant. On a surface of constant phase, which is approximately a conical surface lying in the thickness of the wavepacket, the velocity field describes circles normal to \mathbf{k} with frequency σ . In the limit of small amplitude fluid particles also describe approximately circular trajectories. This surface of constant phase travels across the thickness of the conical wavepacket, from the outer to the inner boundary, with a phase velocity normal to it. Since both the thickness of the wavepacket and the characteristic wavelength are of order of ℓ , the wavepacket merely contains one “crest” and one “trough” of each velocity component.

For very slow oscillations, $\sigma \ll 2\Omega$, the cone aperture θ_g shrinks to zero. In this limit, the resulting wavepacket is reminiscent of a classical Taylor column, whose vertical extent grows as $z = c_g t = 2\Omega t/k$. In this so-called geostrophic limit, the velocity field becomes invariant with respect to the rotation axis, and the fluid velocity follows exactly the velocity of the disturbance inside the cylinder which circumscribes the source (boundary layers actually modify this idealized picture). In the opposite limit, $\sigma \rightarrow 2\Omega$, the double cone degenerates into a plane normal to the rotation axis, but whose horizontal extent grows with a vanishing group velocity. This wavepacket contains a stationary wave, as the result of the interference of the upper and lower wave travelling with opposite phase velocities $\mathbf{c} = \pm 2\Omega/k$. In this planar wavepacket, fluid particles simply make horizontal circles at the natural frequency of the inertial oscillations, 2Ω .

Along the thin conical surface of the wavepacket, a geometric attenuation takes place because of the spatial spreading of energy. Since the energy flux through a sphere centred on the source must be independent of the radius, and considering that the wave energy is localized on an annulus of constant thickness defined by the intersection of the conical wavepacket and the sphere, the kinetic energy $|\mathbf{U}_0(\rho)|^2$ should decrease with the circle perimeter as ρ^{-1} , i.e., the velocity disturbance should decrease as $\rho^{-1/2}$, where ρ is the distance from the source in spherical coordinates.

3 Experimental setup

3.1 The rotating tank and the oscillating disk

The experimental setup is sketched in Fig. 3. It consists in a vertical cylinder, of radius $R = 17.5$ cm and height $H = 42$ cm, mounted on a turntable rotating at a constant frequency $\Omega/2\pi = 0.4$ Hz, with a precision of $\Delta\Omega/\Omega \simeq 6 \times 10^{-3}$. The turntable consists of a large annular gear wheel, 80 cm in diameter, and the rotation is achieved by a lateral pinion, allowing for visualisations from below through the transparent bottom of the tank. A cover is placed below the free surface, preventing from disturbances due to residual surface waves. The rotation of the fluid is set long before an experiment, in order to avoid transient spin-up recirculation flows and to achieve a solid body rotation regime. More details on the turntable may be found in Morize et al. (2005).

The choice of the size and amplitude of the perturbation result from a compromise between several requirements: the far field approximation, a sufficient velocity signal compared to the residual velocity due to the variations of the rotation rate $\Delta\Omega$, and a sufficient attenuation length to avoid multiple reflections. A disk, of radius $R_d = 10.5$ mm and thickness $w = 2.5$ mm, has been used. It is hung at a distance $h' = 130$ mm below the cover by a thin vertical

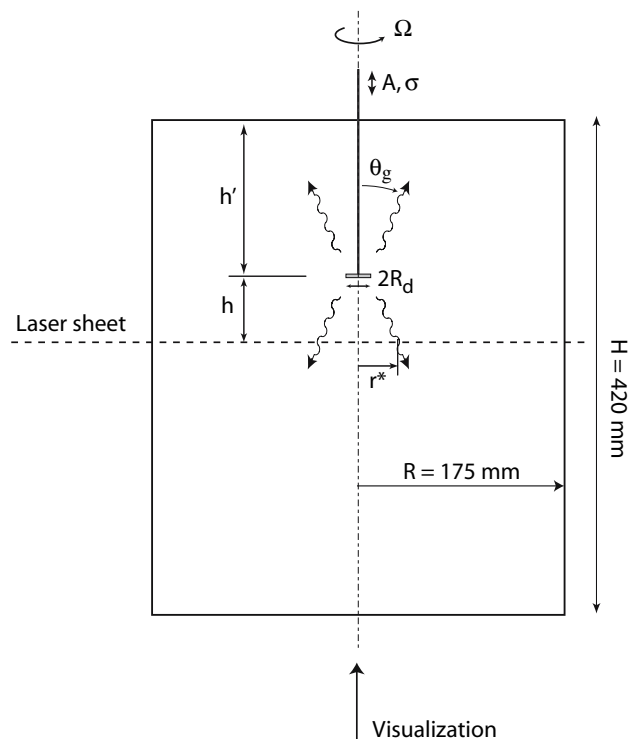


Fig. 3 Experimental setup. The camera (*below*) and the disk are corotating with the tank, while the laser sheet (from *left*) is in the laboratory frame

stem, 1 mm in diameter, that passes through a hole in the cover. The vertical oscillation of the disk, $z(t) = A \cos(\sigma t)$, is achieved by a servo-controlled brushless motor in the laboratory frame, with a coupling device ensuring the transmission of the translation to the rotating frame. As a result, the motion of the disk in the rotating frame is a pure vertical oscillation with no rotation. The amplitude of the oscillation is $A = 5$ mm, and the frequency $\sigma/2\pi$ has been varied in the range 0.10–0.78 Hz, i.e., $\sigma/2\Omega = 0.12$ –0.97.

3.2 Flow regimes and non-dimensional numbers

In the absence of background rotation, two non-dimensional parameters characterize the flow induced by an oscillating bluff body: The Keulegan-Carpenter number, $K_C = \pi A/R_d$, and the Reynolds number, $Re = R_d A \sigma/\nu$. For the present experiments, $K_C = 1.50$ is constant, while Re is varied in the range 30–260. For these values, the flow consists of a periodic shedding of vortex rings on each side of the disk (Tao and Thiagarayan 2003). The modification of this flow pattern by the effects of the rotation is controlled by the Rossby number, which is simply defined here as the frequency ratio $Ro = \sigma/2\Omega$. The detail of the flow near the oscillating disk is not investigated here, and we focus on the resulting inertial waves far from the disk, which exist only for $Ro < 1$.

The *global* versus *local* nature of the inertial waves generated by this forcing may be characterized by comparing the viscous attenuation length along the wavepacket and the size of the container. The damping of inertial waves originates from the shearing motion of the fluid between planes of constant phase, and acts on a timescale $t_v = (2\nu k^2)^{-1}$. The attenuation length may thus be defined from $d_v \simeq c_g t_v$, with c_g the group velocity, i.e.

$$d_v = \Omega/(\nu k^3). \quad (7)$$

Taking the tank height H as the characteristic size of the container, the ratio H/d_v may be written as

$$\frac{H}{d_v} = 2Ek(kH)^3, \quad (8)$$

where $Ek = \nu/2\Omega H^2$ is the Ekman number, which is constant for the present experiments, $Ek = 1.13 \times 10^{-6}$. For $H/d_v \gg 1$, i.e. for $\lambda \ll HEk^{1/3}$, the wave loses most of its energy before reflecting, and the resulting wave pattern may be seen as essentially *local*, with weak confinement effects. Assuming a wavelength of order of the disk diameter (measurements of λ are presented in Sect. 4), the attenuation length is $d_v \simeq 100$ mm, yielding $H/d_v \simeq 4$. Although the condition $H \gg d_v$ is not strictly satisfied, a significant energy fraction is indeed lost before the first reflection. The strongest secondary wave occurs from the

reflection at the cover for small oscillation frequency, and has a relative energy of $\exp(-2h/d_v) \simeq 0.07$, indicating that multiple reflections should not affect significantly the resulting wave pattern.

3.3 Velocity measurements

Instantaneous velocity fields in a horizontal plane located at a distance $h = 5.2R_d = 55$ mm, intercepting the cone at the radius

$$r^* = h \tan \theta_g, \quad (9)$$

are obtained from PIV. The water is seeded by borosilicate spheres, 11 μm in diameter, and the imaged plane is illuminated by a laser sheet of thickness 1 mm produced by a pulsed Nd:YAG laser (25 mJ per pulse). The cylindrical container is immersed into a rectangular water tank, in order to minimize optical distortion of the lighting. Images are acquired from below, through the transparent bottom of the tank, with a camera ($1,280 \times 1,024$ pixels, 4,096 gray levels) located 50 cm below the laser sheet and corotating with the tank. Only a central region of 17.7×14.1 cm² of the flow is imaged. A sampling rate of 8 Hz was used, ensuring a typical particle displacement of the order of 1 mm (5–10 pixels) between two frames. Since the laser source is kept in the laboratory frame, the cylinder and the camera rotate of 18° between two frames, yielding a slight apparent particle displacement even for zero fluid velocity, which contributes to the measurement noise.

Window sizes of 32×32 pixels, with an overlap of 16 pixels, are used for the PIV computations.¹ The final velocity fields are defined on a 80×64 grid, with a spatial resolution of 2.2 mm. A velocity resolution of 0.1 pixel can be achieved using a classical subpixel interpolation scheme for the correlation peak, yielding an uncertainty of 0.12 mm/s. This uncertainty represents about 2×10^{-2} of the velocity amplitude of the inertial wave, and 5×10^{-4} of the velocity of the solid body rotation at the scale of the imaged area.

3.4 Phase average

A residual modulation of the rotation rate of $6 \times 10^{-3}\Omega$, probably originating from a nonconstant friction of the turntable due to a slight misalignment between the rotation axis and the cylinder symmetry axis, superimpose to the mean solid-body rotation Ω . As a result, the measured

¹ DaVis software, by LaVision GmbH, Anna-Vandenhoeck-Ring 19, 37081 Göttingen, Germany, complemented with the PIVMat toolbox for Matlab, <http://www.fast.u-psud.fr/pivmat>.

velocity field is the combination of the inertial wave pattern of interest, of frequency σ , and a background oscillating flow. The velocity signal of the inertial wave being very weak (it is only twice larger than the background flow), it was necessary to phase-average the velocity fields over a large number of periods to extract the mode oscillating at the excitation frequency. For each value of σ , 30 oscillation periods were recorded, each period containing between 6 and 40 velocity fields because of the constant sampling rate.

It must be noted that, since the fundamental frequency of the residual modulation is given by the turntable rotation rate itself, the harmonics $\sigma_{\text{res}} = n\Omega$ are not solution of the dispersion relation (4) for $n \geq 2$, indicating that inertial waves cannot be excited by any harmonics of the residual modulation. As a consequence, the only possible inertial wave excited by the modulation has the fundamental frequency of the turntable, $\sigma_{\text{res}} = \Omega$, and, except for the special case $\sigma \simeq \Omega$ (synchronized oscillation and rotation), which is not considered here, the residual modulation should be cancelled out by the phase average procedure.

4 Results

4.1 Velocity and vorticity fields

Two examples of horizontal velocity fields are shown in Fig. 4, for oscillation frequencies $\sigma/2\Omega = 0.24$ and 0.74 . Only one out of four velocity vectors is plotted for clarity. The vertical component of the vorticity ω_z , computed from second-order centred differences from the horizontal velocity, is also shown on the color background, emphasizing the approximately axisymmetric shearing motion of the wave in the horizontal plane. As expected, the vorticity concentrates into an annulus, defined as the intersection of the conical wavepacket with the horizontal measurement plane, whose radius increases as σ is increased. For these two frequencies, the radii expected from the linear theory are $r^* = h \tan \theta_g = 13.6$ and 60.5 mm, respectively [with $\theta_g = \sin^{-1}(\sigma/2\Omega)$], which is in good qualitative agreement with the pictures. For the lower frequency (Fig. 4a), a weak secondary wave can also be seen at larger radius, originating from a reflection of the primary wave with the cover. Here again, the expected radius, $r^* = (h + 2h') \tan \theta_g = 77.9$ mm, is compatible with the observation.

In Fig. 5, a sequence of six vorticity fields ω_z regularly spaced during one excitation period is shown. An inward propagating circular wave, located in a stationary annular wavepacket, can be clearly seen from these fields.² The

² Animations of vorticity fields are available at the URL <http://www.fast.u-psud.fr/inertialwaves>.

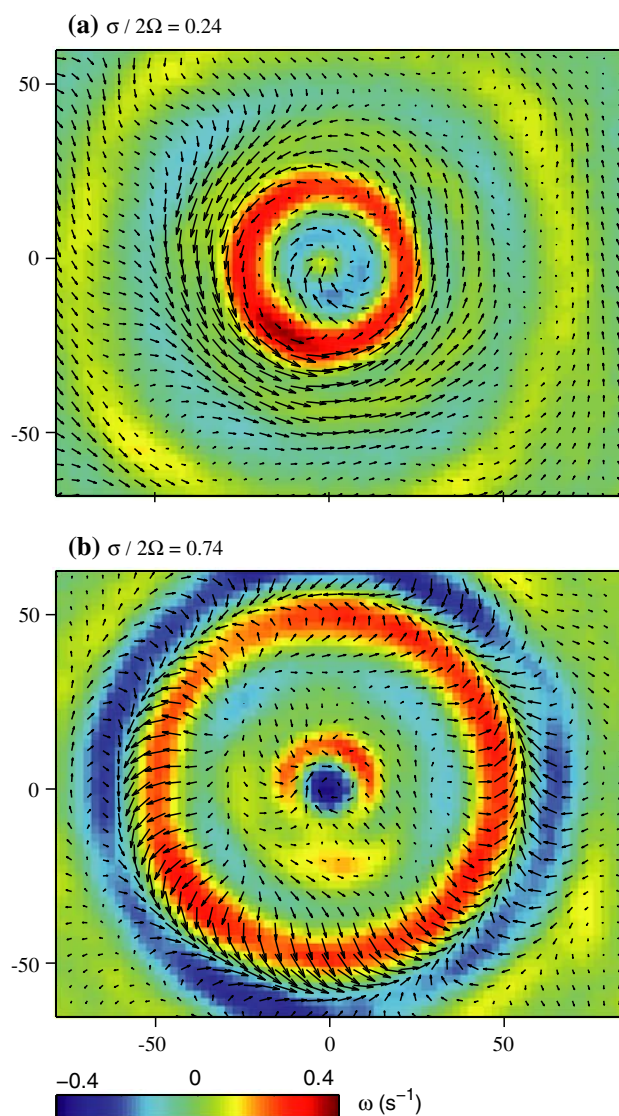


Fig. 4 Examples of velocity field (*arrows*) and axial vorticity field ω_z (color scale), at small (**a**) and large (**b**) excitation frequency. The imaged area is 177×141 mm², and the rotating tank diameter is 35 cm

seemingly paradoxical propagation towards the centre is easily understood from the direction of the wavevector \mathbf{k} normal to the cone surface (see Fig. 2), whose component in the plane normal to the rotation axis is inward. The wavepacket actually contains approximately one crest and one trough, confirming that the width of the wavepacket is indeed of the order of the characteristic wavelength.

It must be noted that a significant level of vorticity is also found near the centre, of the same order or even larger than the vorticity in the cone, on a size comparable to the disk diameter. This feature is not described by the linear inviscid theory in an infinite medium, which

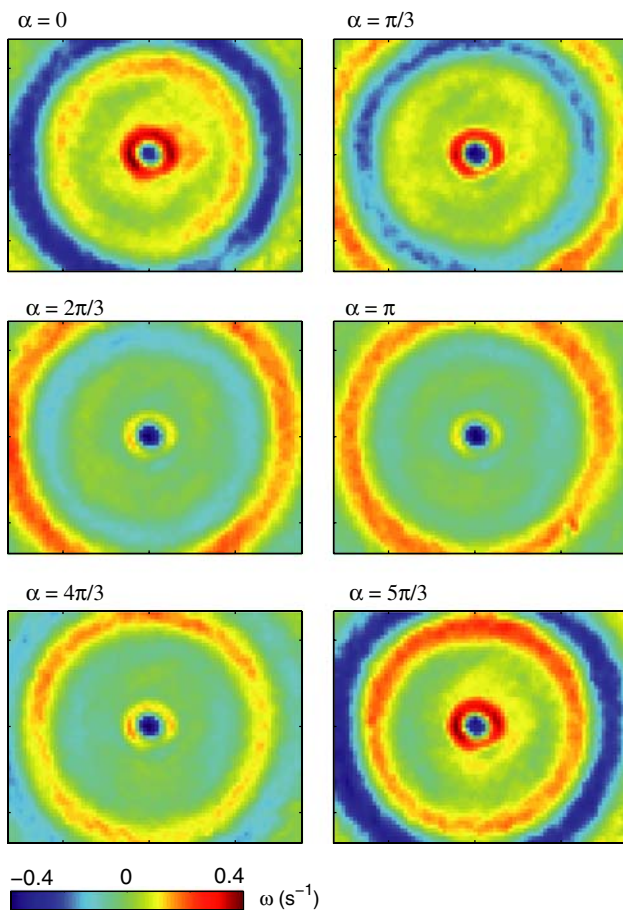


Fig. 5 Phase-averaged vorticity fields, at six equally spaced phase $\alpha = \sigma t = (0..5) \times 2\pi/6$, for $\sigma/2\Omega = 0.83$. One can see approximately one wavelength propagating inward in the stationary envelope of the wavepacket. The scale is the same as in Fig. 4

predicts no fluid motion outside the cone. It resembles a Taylor column, although strict Taylor columns only exist in the limit $\sigma \ll 2\Omega$. At low oscillation frequency, this vorticity patch oscillates with zero mean, in phase with the disk. It may be associated to an alternatively stretched and compressed columnar structure between the disk and the bottom wall (another one is expected above the disk), similar to that observed by Fultz (1959). More surprisingly, at larger frequency, this vorticity patch at the centre also shows a significant nonzero mean (anticyclonic vorticity), as can be seen in Fig. 5. A possible origin for this steady vorticity component is a nonlinear drift, analogous to the Stokes drift for surface waves (Lighthill 1978; Kistovich Yu and Chashechkin Yu 2000). However, the accuracy of the PIV measurements at this scale is probably not good enough to resolve the details of this central vorticity patch, which is left for future investigation, and we focus in the following on the wave in the conical wavepacket.

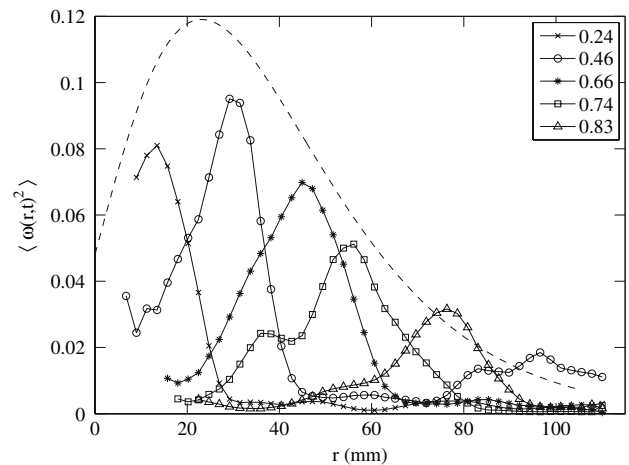


Fig. 6 Wavepacket profiles, defined as the envelope of the squared vorticity profiles (10), for various oscillation frequencies. Note the secondary peak for $\sigma/2\Omega = 0.46$ (circles), due to a reflection of the wave. The dashed line is the law (15), with $d_v = 140$ mm and $\beta = 0.5$, plotted as a function of a shifted radius $r - 15$ mm

4.2 Verification of the dispersion relation

A first verification of the dispersion relation (4) is provided from direct measurement of the radius r^* of the maximum of the wavepacket profile. This profile is computed from the azimuthal and temporal average of the squared vertical vorticity,

$$\langle \omega_z^2(r) \rangle = \frac{1}{T} \int_0^T \left(\frac{1}{2\pi} \int_0^{2\pi} \omega_z^2(r, \phi, t) d\phi \right) dt. \tag{10}$$

Examples of profiles are shown in Fig. 6 for various oscillation frequencies. For increasing frequency σ , the radius of the maximum is shifted outwards. Note also the secondary peak for $\sigma/2\Omega = 0.46$ (circles), associated to a reflection on the cover.

From Fig. 6 the radial location of the maximum, r^* , has been measured, from which the angular aperture of the cone is deduced, $\theta_g = \tan^{-1} r^*/h$. In Fig. 7 are plotted the measurements of $\sin\theta_g$ (asterisks) as a function of the normalised oscillation frequency $\sigma/2\Omega$, showing a good agreement with the linear prediction from the dispersion relation (4).

Another verification of the dispersion relation is provided by the ellipticity of the velocity diagrams, or hodographs, (v_r, v_ϕ) , shown in Fig. 8. Here, the phase- and azimuthally-averaged radial and azimuthal velocity components are measured at the location r^* of maximum vertical vorticity. These diagrams show elliptical patterns, as the result of the projection on the horizontal plane of the tilted circular motion along the cone. As expected, the polarization of the wave is anticyclonic, which corresponds here to an anticlockwise circular translation of the fluid

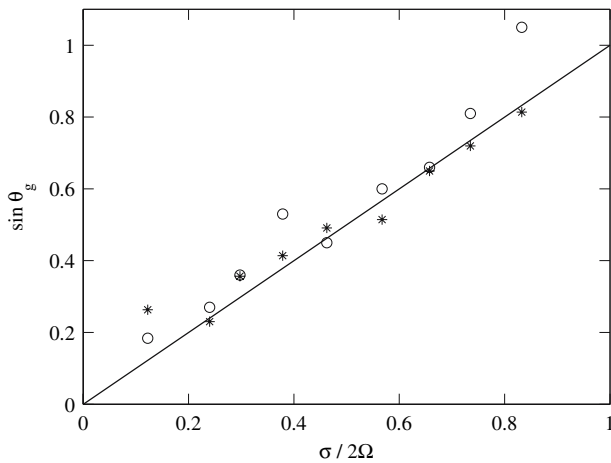


Fig. 7 Cone aperture as a function of the normalized oscillation frequency. *Asterisks* measured from the location of the maximum of the vorticity envelope (Fig. 6). *Circles* measured from the hodograph ellipticity (Fig. 8). The *line* is the prediction from the linear theory, Eq. (4)

particles (the background rotation is clockwise). Measurements of the ellipticity v_r/v_ϕ , which is given by $\sin\theta_g$, are also plotted in Fig. 7 (circles). Here again, an agreement with the linear prediction is obtained, although the data is more scattered than those from the direct measurement of r^* .

4.3 Wavelength

A quantity of interest is the characteristic wavelength λ , or range of wavelengths, of the inertial wave. Since the wavelength is not given by the excitation frequency σ , it has to be selected by some characteristic scale of the disturbance. In the inviscid theory, the size of the disturbance, here the radius and thickness of the disk, and the oscillation amplitude A , are the only relevant lengthscales. In a viscous fluid, λ may also depend on the viscosity, through the thickness of the Stokes boundary layer due to the disk motion $(\nu/\sigma)^{1/2}$, or the thickness of the Ekman boundary layer $(\nu/\Omega)^{1/2}$. The wavelength dependence on those various lengthscales are governed in general by the Reynolds number, the Keulegan-Carpenter number, and the Rossby number.

The wavelength has been measured for different excitation frequencies σ . The apparent wavelength in the horizontal plane, λ_\perp , has been simply estimated from the distance between two vorticity maxima. Since the wavevector component in the plane normal to the rotation axis is $k_\perp = |\mathbf{k}| \cos\theta_g$, the true wavelength $\lambda = 2\pi/|\mathbf{k}|$ is related to the apparent one λ_\perp by

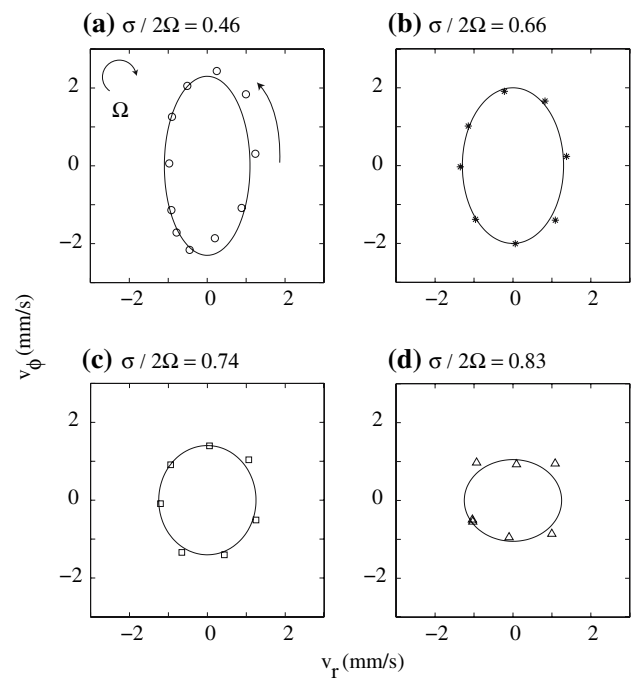


Fig. 8 Phase- and azimuthally-averaged velocity diagram in the plane (v_r, v_ϕ) , measured in the centre of the wavepacket for various frequencies, showing the anticlockwise (i.e., anticyclonic) polarization of the wave. The ellipses in continuous line are fit of the data. The small number of points at high oscillation frequency is due to the constant sampling rate

$$\lambda = \lambda_\perp \cos\theta_g. \quad (11)$$

The apparent and corrected wavelengths are shown in Fig. 9. The angular correction is obtained from the measured r^* , using the relation $\theta_g = \tan^{-1}(r^*/h)$. The corrected wavelength is found to remain approximately constant, $\lambda \simeq 24 \pm 2$ mm, a value close to the disk diameter,

$$\frac{\lambda}{2R_d} \simeq 1.15 \pm 0.1. \quad (12)$$

Although the scaling of λ with respect to the disk radius, disk thickness, oscillation amplitude and viscosity has not been checked, this result indicates that the disk diameter provides here a reasonable estimate for the wavelength, and hence for the wavepacket thickness.

4.4 Estimate for the maximum of ω_z^2

Finally, an estimate for the magnitude of the maximum of the squared vertical vorticity, $\omega_z^2 = \langle \omega_z^2(r^*) \rangle$, may be derived from assumptions about the characteristic vorticity disturbance and geometric considerations. The disk oscillation induces in the near field a disturbance of size δ ,

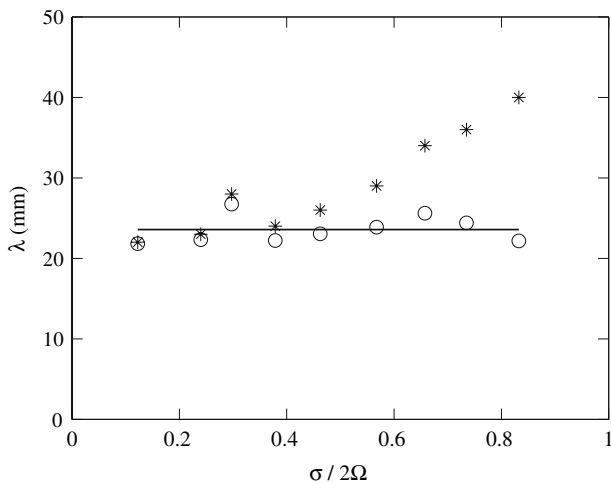


Fig. 9 Apparent wavelength λ_{\perp} (asterisks) and corrected wavelength λ (circles) as a function of the normalized oscillation frequency. The horizontal line shows $\lambda = 24$ mm

which may depend on the details of the flow, and characteristic vorticity $\omega_d = \sigma A / \delta$. For the values of σ in Fig. 6, the Reynolds number Re lies in the range 60–220. In this regime, vortex shedding of size $\delta \simeq A$ is expected, so that the vorticity disturbance is simply given by $\omega_d \simeq \sigma = 2\Omega \sin \theta_g$. The vorticity vector far from the source, ω , is rotating in a plane tangent to the cone, making angle θ_g to the vertical. Its magnitude may be estimated using the ρ^{-1} decrease of the energy due to the spreading along the cone, where ρ is the distance from the source. Using the fact that the wavelength is found to be approximately independent of σ (Fig. 9), the squared vorticity also decreases as ρ^{-1} , and may be written

$$\omega^2(\rho) \simeq \beta \omega_d^2 \frac{R_d}{\rho} \tag{13}$$

for $\rho \gg R_d$, where β is a constant of order unity. Now, since only the vertical component of ω is measured, we write an expression for the maximum of $\omega_z = |\omega| \cos \theta_g$ as a function of r^* . Expressing ρ and θ_g in terms of r^* only, this maximum of the squared vertical vorticity reads

$$\omega_z^{*2} = \beta(2\Omega)^2 R_d \frac{r^{*2} h^2}{(r^{*2} + h^2)^{5/2}}. \tag{14}$$

The growth as r^{*2} for $R_d \ll r^* \ll h$ is due to the increasing energy injected by the oscillating disk as the frequency σ is increased, while the decrease as r^{*-3} when $r^* \gg h$ originates both from the geometric attenuation due to the energy spreading and from the vanishing vertical projection of the vorticity as the cone widens. Although the scale separation in our experiment, $h/R_d = 5.2$, is not large enough to assess these two limiting behaviours, the presence of a maximum in Fig. 6 near $r^* \simeq h$ is indeed

in qualitative agreement with Eq. (14). Other choice for the disturbance size near the disk, e.g. $\delta \simeq R_d$ or $\delta \simeq (v/\sigma)^{1/2}$, would not change significantly the behaviour of Eq. (14) in the range of interest for r^* , in particular the presence of a maximum near $r^* \simeq h$.

The effects of the viscosity may be estimated as follows. Due to the shearing motion of the wave, the energy inside the cone, and hence the squared vorticity, is damped with a factor $\varepsilon = \exp[-2\nu k^2 t]$, where t is the time for a disturbance to travel along a distance ρ from the source. Taking $t \simeq \rho/c_g$, with $c_g = (2\Omega/k)\cos\theta_g$ the group velocity, the damping factor at the radial location $r = r^*$ can be written as $\varepsilon = \exp[-\nu k^3 (r^{*2} + h^2)/(\Omega h)]$. Expressed in terms of the attenuation scale (7), $d_v = \Omega/(\nu k^3)$, the maximum squared vertical vorticity finally reads

$$\omega_z^{*2} = \beta(2\Omega)^2 R_d \frac{r^{*2} h^2}{(r^{*2} + h^2)^{5/2}} \exp\left[-\frac{r^{*2} + h^2}{d_v h}\right]. \tag{15}$$

This law may be compared to the measurements, using $d_v = \Omega/(v(2\pi/\lambda)^3) = 140$ mm from the value $\lambda = 24$ mm obtained in Fig. 9. A reasonable agreement is indeed obtained when Eq. (15) is plotted as a function of a suitably chosen shifted radius, $r - \tilde{r}$, with $\tilde{r} \simeq 15$ mm and taking $\beta \simeq 0.5$ (see the dashed curve in Fig. 6). This virtual origin accounts for near field effects, since the limit $h \gg R_d$ is not satisfied in our experiment. The discrepancies between Eq. (15) and the measured ω_z^* most probably originate from the exact vorticity disturbance near the disk, which may have a more complicated form than the basic scaling $\omega_d \simeq \sigma$. In spite of those uncertainties, one may however conclude that the general behaviour of the maximum of the vorticity envelope in Fig. 6 is reasonably well captured by the present estimate.

5 Conclusion

A series of visualisations of inertial waves, excited by oscillating a small disk in a rotating cylinder, have been performed by means of PIV. This non-intrusive technique allows us to quantitatively investigate the flow field of the wave, by contrast with most previous experiments in similar geometries for which only qualitative observations could be performed. From these PIV measurements, the angle of the conical wavepacket has been measured using two methods, from the radius of the cone and from the ellipticity of the velocity components projected in the measurement plane. Both methods are in good agreement with the dispersion relation for plane waves. The magnitude of the maximum vertical vorticity of the wavepacket, measured in the horizontal plane, is reasonably well described from a simple estimate based on the vorticity

disturbance in the vicinity of the disk and the energy spreading along the cone.

The two conditions to observe *localized* inertial waves in a finite container are (1) the far field approximation, and (2) negligible reflected waves from the walls. Satisfying these two requirements in a laboratory-sized experiment, while keeping an acceptable signal-to-noise ratio, is a difficult task. In the present experiment, these two requirements are only barely satisfied: the distance between the wave source and the measurement plane is $h = (2.3 - 4.2)\lambda$ (depending on the cone angle θ_g), and the attenuation length is $d_v \simeq R/1.8 \simeq H/4.2$, where R and H are the radius and height of the cylindrical container. However, in spite of these limitations, it is remarkable that the essential properties of the inertial waves, in particular the dispersion relation and the wavelength selection, could be verified to within a reasonable accuracy.

Acknowledgments The authors wish to acknowledge A. Aubertin, C. Borget, G. Chauvin, A. Minière and R. Pidoux for experimental help. They also thank J.P. Hulin for fruitful discussions, and G. Tan for help with the manuscript. This work was supported by the ANR grant no. 06-BLAN-0363-01 “HiSpeedPIV”.

References

- Greenspan H (1968) The theory of rotating fluids. Cambridge University Press, London
- Pedlosky J (1987) Geophysical fluid dynamics. Springer, Heidelberg
- Cushman-Roisin B (1994) Introduction to geophysical fluid dynamics. Prentice-Hall, Englewood Cliffs
- Lighthill J (1978) Waves in fluids. Cambridge University Press, London
- Phillips OM (1963) Energy transfer in rotating fluids by reflection of inertial waves. *Phys Fluids* 6(4):513
- Aldridge KD, Lumb L (1987) Inertial waves identified in the earth's fluid core. *Nature* 325:421–423
- Oser H (1958) Experimentelle Untersuchung über harmonische Schwingungen in rotierenden Flüssigkeiten. *Z Angew Math Mech* 38(9/10):386–391
- Fultz D (1959) A note on overstability and the elastoid-inertia oscillations of Kelvin, Soldberg, and Bjerknes. *J Meteorol* 16:199–207
- McEwan AD (1970) Inertial oscillations in a rotating fluid cylinder. *J Fluid Mech* 40:603–639
- Ito T, Suematsu Y, Hayase T, Nakahama T (1984) Experiments on the elastoid-inertia oscillations of a rigidly rotating fluid in a cylindrical vessel. *Bull JSME* 27(225):458–467
- Manasseh R (1996) Nonlinear behaviour of contained inertia waves. *J Fluid Mech* 315:151–173
- Duguet Y (2006) Oscillatory jets and instabilities in a rotating cylinder. *Phys Fluids* 18:104104
- Beardsley RC (1970) An experimental study of inertial waves in a closed cone. *Stud Appl Math XLIX(2):187–196*
- Malkus WVR (1968) Precession of the earth as the cause of geomagnetism. *Science* 160:259–264
- Maas LRM (2001) Wave focusing and ensuing mean flow due to symmetry breaking in rotating fluids. *J Fluid Mech* 437:13–28
- Manders AMM, Maas LRM (2003) Observations of inertial waves in a rectangular basin with one sloping boundary. *J Fluid Mech* 493:59–88
- Godeferd FS, Lollini L (1999) Direct numerical simulations of turbulence with confinement and rotation. *J Fluid Mech* 393:257–308
- Morize C, Moisy F, Rabaud M (2005) Decaying grid-generated turbulence in a rotating tank. *Phys Fluids* 17:095105
- Tao L, Thiagarayan K (2003) Low KC flow regimes of oscillating sharp edges. I. Vortex shedding observation. *Appl Ocean Res* 22:281–294
- Kistovich Yu V, Chashechkin Yu D (2000) Mass transport and the force of a beam of two-dimensional periodic internal waves. *J Appl Math Mech* 65(2):237–242